Polymer 334 (2025) 128768

Contents lists available at ScienceDirect

Polymer

journal homepage: www.elsevier.com/locate/polymer

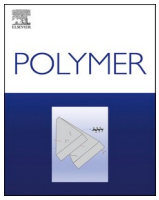

Tunable dual-curing acrylic/epoxy systems for 3D printing with enhanced joint performance via carbon nanotubes

A.A. Escriba-Flores [a], X. Fernández-Francos [b], F. Ferrando [a], A. Fabregat-Sanjuan [a,*]

[a] Department of Mechanical Engineering, Universitat Rovira i Virgili, Av. Països Catalans 26, 43007, Tarragona, Spain
[b] Thermodynamics Laboratory, ETSEIB, Universitat Politècnica de Catalunya, Av. Diagonal 647, 08028, Barcelona, Spain

ARTICLE INFO

Keywords:
Dual curing
DLP 3D printing
Additive manufacturing
Nanoadhesive
High tensile strength
MWCNTs-COOH

ABSTRACT

This study presents a novel dual-curing strategy for low-viscosity, high-performance acrylic/epoxy systems, which enables precise control over the final density of the co-network structure and its thermo-mechanical properties. Unlike conventional acrylate/epoxy dual-curing systems, this new strategy incorporates a long chain extender (polyethylene glycol) covalently bonded within the epoxy network to specifically reduce the crosslinking density achieved in the second curing stage. This allows for fine-tuning of the material's mechanical properties, facilitating adjustments to the elastic modulus from 3 MPa to 2500 MPa and achieving maximum tensile strength values of 80 MPa, while maintaining a low viscosity of less than 35 mPa s, making it ideal for 3D printing vat photopolymerization applications. Additionally, the material exhibits good thermal stability and excellent printed components resolution, thereby opening a wide range of design options for achieving optimal configurations related to mechanical preferences and precise geometric accuracy. The work further includes an analysis of tensile strength in bonded joints, which is a crucial parameter in structural design, particularly for the fabrication of large parts through bonding. Moreover, the project proposes the incorporation of functionalized multi-walled carbon nanotubes (MWCNT-COOH) to enhance interfacial adhesion between phases.

1. Introduction

The 3D VAT photopolymerization printing has gained significant interest in recent years within the scientific community due to its remarkable capacity to fabricate intricately shaped components without the necessity for specialized molds or tools [1]. These advantages hold considerable promise across diverse industries, including aerospace [2], automotive [3], medical [4], and general manufacturing [5]. The evolution of this technology advances in parallel with the development of the materials it employs, primarily consisting of monomers like acrylates [6], methacrylates [7], epoxides [8] or siloxanes [9].

Furthermore, commercially available materials cover a wide range of mechanical properties, from those used for simple modeling to materials with potential for structural applications and high mechanical and thermal performance [10]. The mechanical properties of the final materials depend on the monomers or oligomers used in their formulation. In general, monomers with small molecular size generally lead to formulations with reduced viscosity and faster curing kinetics, that can be easily printed to complex geometries with the help of suitable supports, but also offer lower mechanical performance [11]. On the other hand, formulations with larger molecular masses offer better mechanical properties but also have higher viscosity and longer processing times [11]. Despite the wide range of materials available, producing large-scale parts with structural integrity remains a challenge. This difficulty arises from phenomena such as swelling or shrinkage, which lead to fractures between layers due to the internal stresses generated during the photopolymerization process [12]. To overcome these issues, one potential strategy could involve printing components separately and subsequently bonding them together, either with the same material formulation or a compatible adhesive. Evaluating the tensile, bending, and shear strengths in bonded parts is essential for ensuring structural strength. While there are numerous examples of polymer adhesion in the literature [13,14], there is still a lack of documented solutions specifically suited for VAT photopolymerization 3D printing. Some studies have employed polymer pieces as adherends, with resins serving as adhesives, yet comprehensive studies focused on this area remain limited [14,15]. For instance, Zoran et al. [16] demonstrate this concept, even though employing a different printing method, namely Fuse

* Corresponding author.
E-mail addresses: armandoalfredo.escriba@urv.cat (A.A. Escriba-Flores), xavier.fernandez@upc.edu (X. Fernández-Francos), f.ferrando@urv.cat (F. Ferrando), a.fabregat@urv.cat (A. Fabregat-Sanjuan).

https://doi.org/10.1016/j.polymer.2025.128768
Received 25 April 2025; Received in revised form 23 June 2025; Accepted 2 July 2025
Available online 3 July 2025

Deposition Modeling (FDM). The study successfully produced Polyethylene terephthalate glycol (PETG) parts, which underwent testing in single lap configurations. These parts were analyzed using a commercial adhesive (LOCTITE® 3090™ from Henkel, Düsseldorf, Germany) across various thickness configurations. This case underscores the necessity of exploring joint techniques in printed parts for structural applications. Additionally, similar cases are documented by Khosravani et al. [17] discusses an extensive review of FDM-printed parts and concludes that most of the documents are related to different approaches analyzing lap-shear configurations, offering low relevance to 3D VAT photopolymerization and showing a lack of studies related with tensile stress 3D printing polymer joints. Another example highlighting the significance of such approaches is the work of Dahmen et al. [18]. In their study, they crafted a composite using commercial epoxy resin EPX 81 from Carbon, bonded with reinforcement material NB4030-D from Mitsubishi Chemical Carbon Fiber and Composites, Inc. This configuration is particularly intriguing given that EPX 81 resin is a dual-cure resin. The study meticulously analyzed two types of joints: one in a lap-shear configuration and the other in a T-joint structure. Notably, both joints utilized the commercial EPX 81 resin along with two other commercial resins activated by temperature reaching interesting results using resins such an adhesive in printed parts. This research underscores the potential for producing and bonding printed parts to construct structures capable of withstanding rigorous structural demands, underscoring the importance of joint property analysis.

An interesting approach is the use of sequential dual-curing processing in 3D-printing applications. Typically, the UV-triggered (meth) acrylate radical polymerization that is activated in the 3D-printing stage, is combined with a second polymerization reaction that is activated in a second curing stage after the printing process [19,20]. Such an approach is commonly utilized to enhance or modify the mechanical properties of vat polymerization printed parts, aiming to ensure material reactivity to light without significant deformations during printing, thereby facilitating rapid and damage-free part formation [21,22].

Dual-curing processing leads to two different structures at the end of each curing stage: the intermediate one, which can be designed according to processing requirements, and the final one, which should meet the requirements of the application [20,23,24]. In the context of 3D-printing, it has been proposed that the existence of this intermediate state after 3D-printing can be used to produce complex parts from the assembly or reshaping of single printed specimens, making use of the intermediate adhesion and mechanical compliance of the intermediate material [22,25]. It should be recalled that the intermediate state of the material contains unreacted residual groups associated with the second curing stage [21,26]. These unreacted residual groups have the potential to form covalent bonds on the surface of the part, thus opening up new possibilities for creating joints capable of withstanding significant structural stresses. This aspect of the intermediate process offers a valuable alternative for enhancing the strength and durability of parts manufactured using this technology. However, successful application of these concepts requires a specific design of the network architecture and properties of the intermediate stage after the 3D-printing stage, which is an issue that has been generally overlooked so far. A suitable choice of monomers participating in the 1st and 2nd curing stages could lead to intermediate flexible materials i) capable of withstanding significant deformations, enabling safe handling and reshaping, ii) having remarkable intermediate adhesion due to the presence of unreacted moieties and monomers, and iii) leading to final materials with tunable properties suitable for a wide range of applications.

Several research efforts have begun to explore this potential [23,24]. For instance, a compelling example was recently presented by J. Kopatz et al. [27], who developed a dual-curing resin for DIW 3D printing that allows the production of parts with high glass transition temperatures. Their formulation is based on a dimethacrylate monomer, which polymerizes during the first curing stage, forming a printable, crosslinked acrylate network whose rigidity depends on the amount of acrylate phase present. For the second stage, they incorporated two commercial epoxy resins: EPON 828 (a bifunctional epoxy) and Tactix 724 (a trifunctional epoxy). By tuning the amount of dimethacrylate, they optimized the printing process and evaluated the thermal, thermomechanical, and mechanical properties of the final parts. Their approach allowed them to achieve Tg values between 120 °C and 220 °C, attributed to the epoxy content and the densification that results from the formation of two interpenetrating networks.

Despite these promising outcomes, the study by Kopatz et al. leaves certain aspects open to further exploration, particularly concerning the intermediate state, whose mechanical behavior plays a critical role in dual-curing systems. For instance, the intermediate stage was not mechanically characterized in depth, despite its potential impact on post-processing steps such as reshaping or bonding. Additionally, while the system demonstrates control over Tg in the final stage, it does not offer evidence of broader tunability in mechanical behavior, e.g., the ability to switch from flexible to rigid states depending on formulation, nor does it cover a wide spectrum of final property profiles. These limitations underscore the need for further investigation into how intermediate state design can influence final performance and expand the versatility of dual-curable systems.

Given these limitations in controlling the mechanical properties throughout the curing stages, especially in the intermediate state critical for post-processing, recent approaches have focused on integrating nanomaterials into polymeric matrices [28] This strategy aims to improve joint strength and mechanical performance by leveraging the unique properties of nanomaterials in adhesion and network reinforcement. Specifically, these materials can promote stronger bonding when used as adhesives between 3D vat photopolymerization printed components, which act as adherends. It is widely recognized that the inclusion of nanomaterials can enhance electrical, thermal, and mechanical properties, thereby unlocking novel avenues for application [29–32]. Existing literature demonstrates the utilization of various systems incorporating nanoparticles into polymeric matrices, such as epoxy resins, which are subsequently employed as adhesives for bonding metal or plastic matrices [33,34]. However, current analyses predominantly focus on shear stress, primarily evaluated via lap shear tests. This underscores the necessity of adopting methodologies that can be used to analyze stresses within joints formed by vat photopolymerization-printed parts.

A previous study describes a dual-cured acrylic/epoxy system, which combines the homopolymerization processes of acrylates and methacrylates under ultraviolet (UV) radiation in 3D printing, together with the cationic ring-opening of epoxide groups, activated by a latent thermal cationic initiator [21]. Each of these processes is triggered in a controlled and sequential way, ensuring the ability to form printed parts with specific characteristics. The optimization of the interaction between the two networks is achieved through the addition of an acrylic chain extender containing an –OH group. This chain extender i) enables the formation of a highly stretchable intermediate material at the end of the 1st radical homopolymerization reaction and ii) facilitates the formation of covalent bonds between the two networks, acting as a homogenizer that integrates the two structures. These hybrid acrylic/epoxy polymer networks can be conceptualized as a volume occupied by densely or loosely crosslinked systems, with the capacity of being largely modified depending on the mechanical properties and the volume occupied by each network.

In a previous work [35], the influence of a coupling agent in an acrylic/epoxy system was explored. The system demonstrated excellent performance in terms of reactivity, latency, thermal stability, low viscosity, 3D printability, and mechanical properties in both its intermediate and final states. Additionally, its mechanical behavior under tensile and direct shear conditions was evaluated, both in bulk form and in adhesive joints. However, the study did not explore the effect of the network structure and mechanical properties on adhesion strength, nor the interfacial effects when joining different materials. Moreover, the

potential for enhancing joint performance in assemblies from dual-cured 3D-printed parts was not considered. Likewise, the design of crosslinked networks through the incorporation of reactive species and post-curing reactions remains unexplored. Finally, the use of nano-fillers with surface functionalization, capable of forming covalent bonds within the adhesive matrix, was not addressed, despite their potential to improve their mechanical performance as well as adhesive properties.

In this work we propose a different strategy to modify the crosslinking density of dual-cured hybrid acrylate/epoxy polymer networks, with the purpose of fine-tuning the final material properties. A base acrylic resin with a hydroxyl methacrylate component as coupling agent will be combined with an epoxy component and a linear polyol. This latter component is introduced to further promote chain extension and chain-transfer events during the 2nd curing stage, following the so-called activated monomer (AM) mechanism, thus reducing the final crosslinking density and acting as an internal plasticizer. Scheme 1 summarizes the different processes and reactions taking place in this hybrid system.

Herein, this study aims to address four primary experimental analysis points that collectively advance the current state of dual-curing systems in vat photopolymerization 3D printing. Firstly, it involves the development of two systems capable of producing high-resolution, low-viscosity printed parts. Secondly, it examines the incorporation of a crosslinking controller to effectively modify the mechanical and thermomechanical properties of the final curing state for two similar systems, demonstrating unreported control over the final mechanical properties across a wide range from flexible to rigid materials in 3D printing formulations. Thirdly, it proposes the detailed analysis of the joints produced by covalent bond formation from residual reactive groups present in the intermediate state, as well as the incorporation of adhesive solutions from the same chemical families at part interfaces. This aspect is largely unexplored in the literature but critical for scalable and structurally reliable 3D printed assemblies. Finally, it explores the incorporation of functionalized multi-walled carbon nanotubes (MWCNTs-COOH) into the joints, investigating their potential synergistic effect in enhancing adhesion and mechanical performance beyond conventional approaches. The comprehensive characterization includes cure kinetics, processing-related physical properties, and mechanical testing at both intermediate and final curing stages, thus providing an understanding of the dual-curing process and its potential for tailored, high-performance applications.

2. Experimental part

2.1. Formulations

The formulation of the dual-curing systems combines a commercial acrylic resin Spot-E, sourced from Spot-A Materials (Barcelona, Spain), which contains mono- and di-(meth)acrylates groups. In addition, it incorporates epoxy resins, including EPx (bis(3,4-epoxycyclohexylmethyl) adipate) and EPy (3,4-Epoxycyclohexylmethyl 3,4-epoxycyclohexanecarboxylate), along with HEA (2-Hydroxyethyl acrylate,

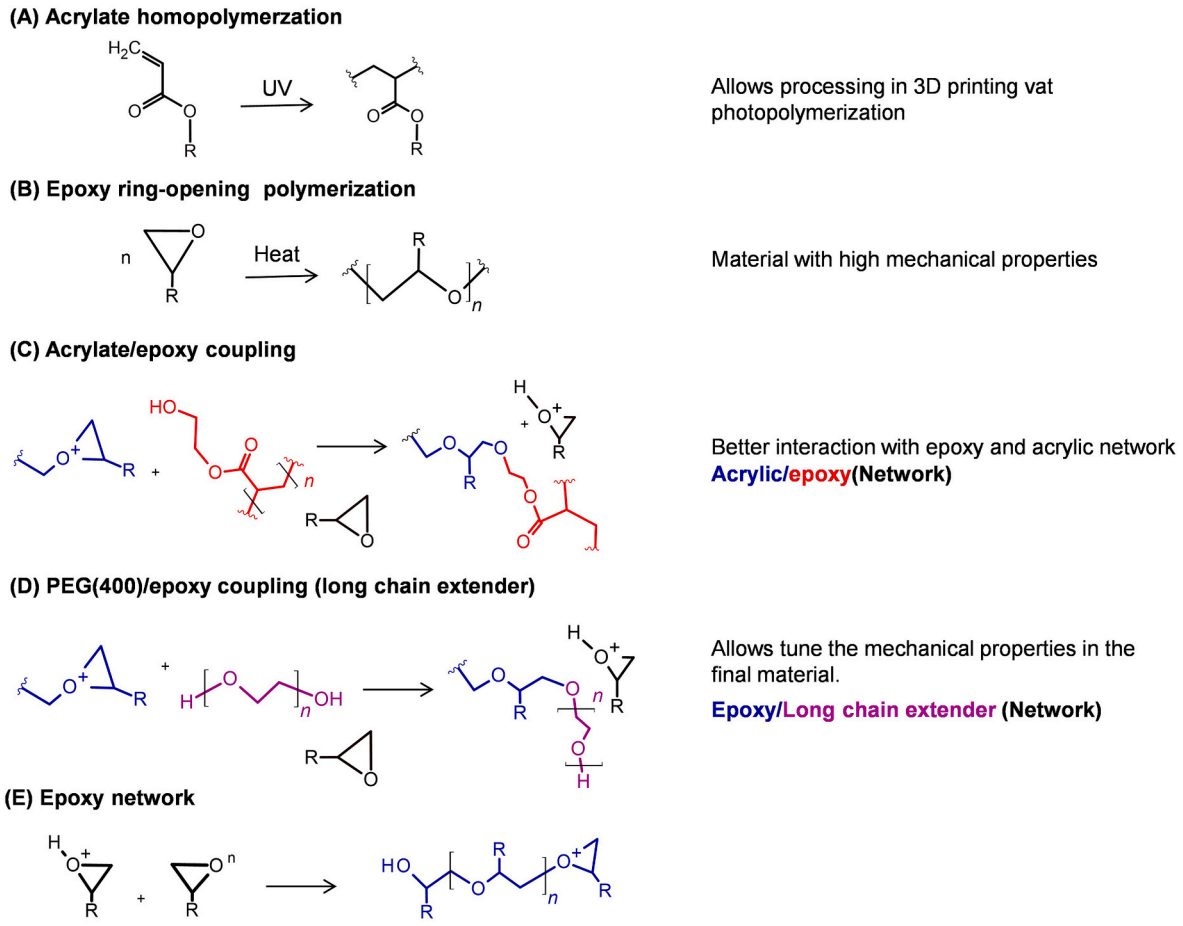

Scheme 1. (A) The process of forming an acrylic network activated by UV radiation is illustrated, leading to the creation of a homopolymer. (B) Similarly, but this time activated by heat, the polymerization of epoxide groups in an epoxy resin is observed. (C) Next, the joining of the two networks, both epoxy and acrylic, is shown through the nucleophilic reaction of the –OH group present in the acrylic resin. (D) Then, the connection between the epoxy network and the chain extender (PEG 400) is detailed. As with the acrylic resin, this reaction is carried out by the nucleophilic attack of the –OH group present in PEG. (E) Finally, the simple growth of the epoxy network is demonstrated.

116.12 g/mol) and HEMA (2-Hydroxyethyl Methacrylate, 130.1 g/mol) serving as bonding agents. PEG (Poly(Ethylene Glycol), 400 g/mol) acts as a chain-transfer agent and internal plasticizer. Additionally, TEA (triethanolamine, 149.2 g/mol), PC (propylene carbonate, 102.1 g/mol); Phenylbis(2,4,6-trimethylbenzoyl) phosphineoxide (BAPO) functions as photo-initiator, supplied by Sigma-Aldrich (Schnelldorf, Germany). In addition, radical thermal initiator 1,1-Bis(tert-amylperoxy) cyclohexane (Luperox 531M60) was provided by Arkema (Günzburg, Germany). Cationic initiator K-PURE CXC-1612 was provided by King Industries (Norwalk, Connecticut, USA).

The formulations detailed in this project are presented in Tables 1 and 2. Each formulation was calculated as a percentage of the total weight. Moreover, 2.00 % wt (50 % wt K-PURE CXC-1612, 5 % TEA and 45 % of PC) of a thermal cationic initiator solution was used, along with 2.70 % wt of BAPO as an additional photo-initiator in both cases.

The different formulations were prepared by accurately weighing each component using a precision scale and homogenization by hand stirring followed by 10 min under magnetic stirring. Subsequently, the mixture was allowed to rest for 10 min before proceeding to the processing steps within the printer.

2.2. a3D-printing and preparation of samples

Specimens were printed using an ASIGA MAX-UV 3D printer (Sydney, Australia) equipped with a UV light source at 385 nm. Samples were printed using a layer thickness of 0.07 mm with an intensity set at 4.77 mW/cm2, and an exposure determined from the Jacobs curve of the formulations.

To construct the Jacobs working curve, three samples of each formulation underwent radiation at an intensity of 4.77 mW/cm^2, utilizing a wavelength of 385 nm (on the ASIGA-MAX-UV 3D printer), with exposure durations ranging from 10 to 60 s within a circular section measuring 10 mm in diameter. The thickness or curing depth (Cd) was subsequently measured using a micrometer. For each formulation, a straight line was plotted on a logarithmic scale. The behavior of the curve was modeled by the following Equation (1):

$$C_d = D_p \, ln\left(\frac{E}{E_c}\right) \quad (1)$$

Where, C_d (μm) represents the cure depth/thickness of the sample, E_c is the critical energy, and E the maximum energy (mJ·cm^{-2}) of the radiation incident on the surface. D_p (μm) signifies the penetration depth of the light. When C_d is plotted against Emax on semilogarithmic axes, it exhibits a linear curve known as the Jacobs working curve. E_c can be determined by the point where this curve intersects the x-axis, while D_p is calculated from its slope.

Printed parts were rinsed in isopropanol and underwent UV curing using a DentalFarm UV curing oven (photopol VAC + GAS) (Pordenone, Italy). This UV curing process lasted for 10 min under a pressure of −0.09 MPa and an intensity of 200W, in order to complete the reaction of acrylate and methacrylate groups from Spot-E, and HEMA/HEA coupling agents, leading to the intermediate material. The second curing stage was carried out at 150 °C for 4 h in a convection oven in order to ensure complete reaction of all epoxy groups and achieve the final material properties.

Table 1
Constitution and nomenclature of each formulation in the system HEAEPxPEG. The composition in the different components is given in wt.%.

Code	HEAEPxPEG0	HEAEPxPEG5	HEAEPxPEG10	HEAEPxPEG20
Spot-E	20	20	20	20
HEA	40	40	40	40
Epoxy (EPx)	40	35	30	20
PEG	0	5	10	20

2.3. Thermal and physicochemical characterization

To investigate the kinetics of the initial curing stage, the photocurable solution was placed in a modified Mettler DSC 821e calorimeter (Greifensee, Switzerland), fitted with a Hamamatsu Lightning Cure LC5 (medium-pressure Hg–Xe lamp), (Hamamatsu, Japan), using two light-guides — one directed at the sample and the other at the reference. Approximately 2 mg of the solution was placed in open aluminum pans under a nitrogen atmosphere. Samples were stabilized at 30 °C for 2 min before exposure, irradiated for 8 min at 30 °C with a light intensity of 20 mW/cm^2, then kept in the dark for an additional 2 min. The experiments were performed under a nitrogen flow (50 ml/min). To account for the thermal effects of UV irradiation during photocuring, each sample underwent two consecutive runs, with the second run being subtracted from the first to determine the polymerization rate and the reaction heat. Thermal analysis for the second curing stage was performed using a DSC (Differential Scanning Calorimetry, DSC 3+ by METTLER TOLEDO), (Greifensee, Switzerland). Samples ranging from 0.010 to 0.025 g of the intermediate material were used for this analysis, with temperature parameters covering from −50 °C to 250 °C at a rate of 10 °C/min. A second scan was also performed to determine the glass transition temperature of the fully cured material.

To assess the thermal stability of the samples, thermogravimetric analysis was conducted using a Mettler Toledo TGA/DSC 1 Star System (Greifensee, Switzerland). Samples of ca. 10 mg were placed in alumina crucibles covered with a pierced lid and were heated at 10 °C/min from 25 °C to 700 °C under nitrogen atmosphere.

For thermomechanical analysis, a DMA Q800 by TA Instruments (New Castle, Delaware, USA) was utilized. Samples with dimensions of 10 × 50 × 5 mm were employed for this experiment. The experiment was conducted in single cantilever mode with an oscillation strain of 0.1 %. Samples were initially held at −20 °C for 10 min and subsequently subjected to a ramp of 3 °C/min until reaching a temperature of 200 °C. The glass transition temperatures of the materials were determined as the tan δ peak of the α-relaxation.

Infrared spectroscopy was carried out using a Bruker Vertex 70 FTIR spectrometer (Billerica, Massachusetts, USA), equipped with an attenuated total reflection (ATR) accessory (GoldenGateTM by Specac Ltd.), (Orpington, United Kingdom). Spectra were collected in the mid-infrared region across a spectral range from 4000 cm^{-1} to 600 cm^{-1}. 20 scans were averaged for each spectrum. Samples of the uncured liquid, partially cured and fully cured materials were analyzed.

Raman spectroscopy was performed using a Raman Renishaw InVia by Renishaw plc. (Wotton-under-Edge, Inglaterra). A 785 nm laser was employed for the detection of the presence of MWCNTs in the formulations.

2.4. Viscosity measurement

The viscosity as a function of shear rate was assessed using a TA Instruments HR20 rheometer (New Castle, DE, USA) in a plate-plate setup. To avoid cross-contamination between measurements, disposable aluminum plates with a 25 mm diameter were utilized. The experiments were performed at 30 °C, maintained by an electrical heating plate (EHP) system and keeping a gap of 0.02 mm, with shear rates spanning from 0.10 to 3000 s^{-1}.

2.5. Tensile test

Tensile tests were conducted following the procedures outlined in ISO 527-1/2 standards, employing a loading rate of 1.5 mm/min and a 500 N load cell using Shimadzu's AGS-X series 10 kN Tabletop model (Shimadzu Scientific Instruments), (Kyoto, Japan). Deformation measurements were taken using a video extensometer, TRViewX (Shimadzu Scientific Instruments), and the entire setup was operated using Trapezium X Testing Software (Shimadzu Scientific Instruments).

Table 2
Constitution and nomenclature of each formulation in the system HEMAEPyPEG. The composition in the different components is given in wt.%.

Code	HEMAEPyPEG0	HEMAEPyPEG5	HEMAEPyEG10	HEMAEPyPEG20
Spot-E	20	20	20	20
HEMA	40	40	40	40
Epoxy (EPy)	40	35	30	20
PEG	0	5	10	20

2.6. Evaluation of joint performance

Halves of specimens for mechanical testing were printed and post cured in the UV oven in order to reach a controlled intermediate state, as described above. Joined test specimens were prepared following the procedure illustrated in Fig. 1, using a liquid resin interphase between the two halves in order to improve the contact. The joint area was irradiated in order to ensure complete reaction of the acrylic groups and then the whole specimen was post cured in a convection oven in order to activate the 2nd reaction and ensure covalent bonding across the interphases. The full description can be found in [35].

In order to improve the adhesion strength, the liquid adhesive used at the interphase between the printed parts was modified by incorporation of carboxyl-functionalized multi-wall carbon nanotubes (MWCNTs). The functionalization of the nanotubes with –COOH grafts was accomplished through a well-established chemical treatment [36,37]. Initially, 250 g of nanotubes were placed in a round-bottom flask, to which a solution of nitric acid and sulfuric acid in a ratio of 1:3, respectively, was added. The nanotubes underwent magnetic stirring at 70 °C for a period of 6 h. Subsequently, the excess acid was removed, and the nanotubes were washed with distilled water eight times until reaching a neutral pH. Then, the nanotubes were dried at 80 °C for 24 h to ensure the removal of any residual moisture. Scheme 2 illustrates the reactions that occur during this process, showing how the –COOH groups facilitate chemical bonding with epoxy resins.

For the preparation of the nano-adhesive, we employed MWCNTs-COOH at concentrations of 0.1 wt%, 0.5 wt%, and 0.8 wt%, utilizing the solution matrix formulation of HEMAEPyPEG0. The formulations were prepared in a round-bottom flask, and an ultrasonic treatment in a bath for 2 h was applied to achieve an optimal dispersion of the nanotubes.

3. Results and discussion

3.1. Thermal and physicochemical characteristics

The thermograms obtained by photo-DSC shows a fast photocuring process, where it can be observed that the samples were fully cured after 1 min of irradiation (see Figure S-1 in Supplementary material). The samples with HEA exhibited a faster reaction compared to those with HEMA, as acrylates are more reactive than methacrylates. It is also observed that HEMA systems are accelerated with increasing presence of PEG, which could be related to the reported accelerating effect observed in systems with hydroxyl-ended polyethylene glycol side chains [38] Fig. 2 (A) and 2 (B) present the thermograms of the DSC analysis of 2nd curing stage of HEAEPxPEG and HEMAEPyPEG systems, respectively, highlighting the effect of PEG content in each. It was observed that all HEAEPxPEG systems had an onset temperature around 130 °C, while all HEMAEPyPEG systems had an onset temperature around 120 °C (see Table 3). These results evidence that the latency of the 2nd reaction stage [39] was not affected by the presence of PEG, However, the reactivity of EPx, which contains two ester groups, is slightly lower than that of EPy, which contains a single ester group, likely due to the influence of the additional ester group. [40]. Table 3 shows there is a decrease in the enthalpy of reaction with increasing PEG content, due to the decreasing presence of epoxy component. The enthalpy of reaction was lower for HEAEPxPEG systems due to the larger molecular size of EPx (ca. 200 g/eq) in comparison with EPy (ca 130 g/eq). Additionally, thermogravimetric analysis provided valuable insight into the thermal stability of each solution Fig. 2 (C) and 2 (D). It was found that both systems exhibited a single degradation stage, indicating good interaction between the components in the crosslinked network. Regarding thermal degradation, excellent stability was observed: for both systems, degradation began around 250 °C. Importantly, PEG did not exhibit a significant influence on this thermal degradation process.

The loss factor of the fully cured materials (tan(δ) = E''/E') is shown in Fig. 3. It is observed that the presence of PEG decreases the tan(δ) peak temperature of the loss factor for both HEAEPxPEG and

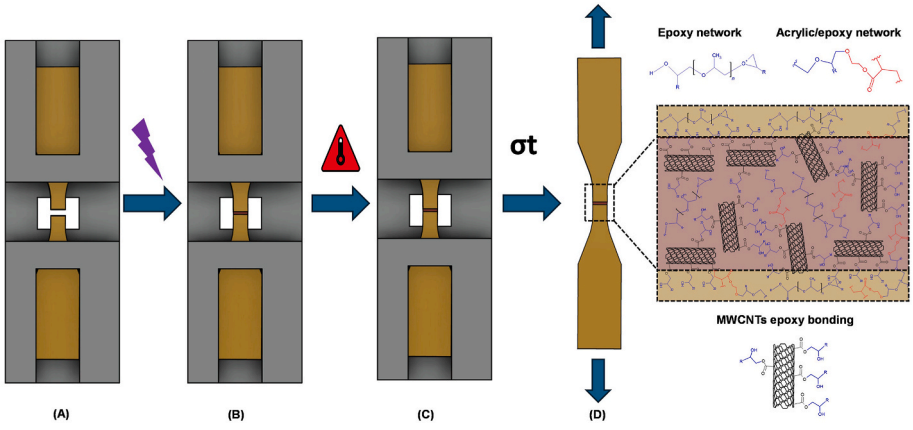

Fig. 1. (A) Represents both printed parts placed on a special tooling to hold them and control the gap distance. (B) The incorporation of the adhesive and nano-adhesive at the interface of the parts is illustrated. It shows how the piece is irradiated to generate the intermediate joint. (C) The sample is subjected to 180 °C for 3 h to ensure curing. (D) Tensile tests are performed and a schematic representation of the nanoadhesive composition is provided, describing the role of the acrylic and epoxy networks as well as the functionalized nanotubes.

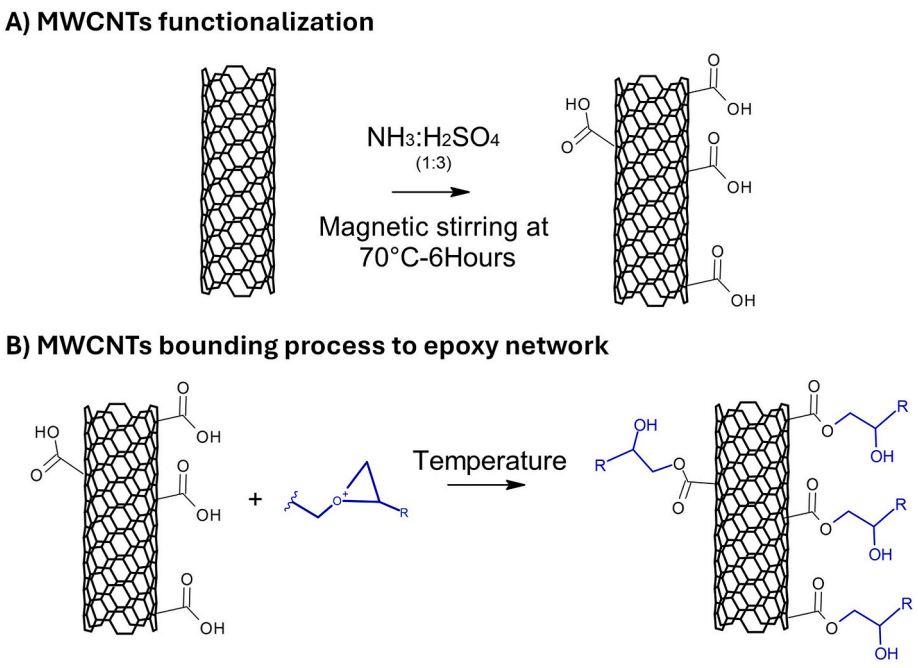

Scheme 2. (A) Functionalization of Multi-Walled Carbon Nanotubes (MWCNTs) with acid treatment. (B) MWCNTs bonding with Epoxy network.

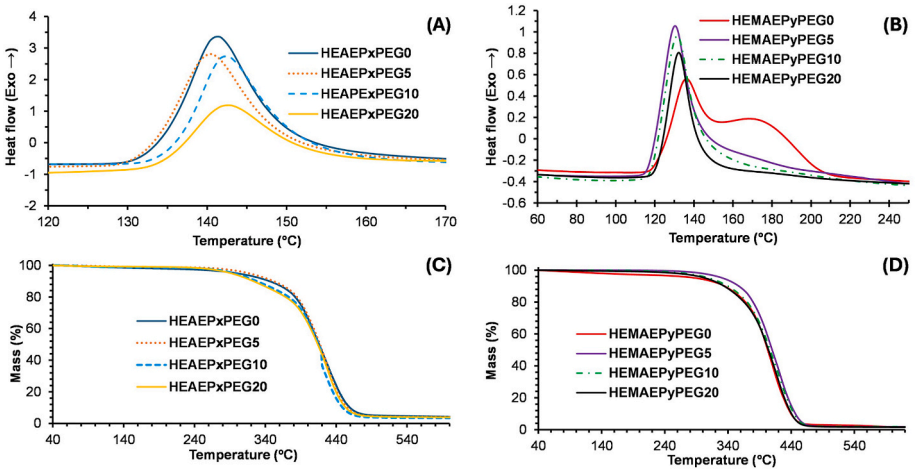

Fig. 2. (A–B) kinetic reaction and (C–D) thermal stability of all formulations evaluated.

Table 3
Summary of calorimetric data obtained from the DSC analysis of the 2nd reaction stage.

Formulation	Start temperature (°C)	Peak temperature (°C)	Heat release (J/g)
HEAEPxPEG0	130.25	141.33	166.04
HEAEPxPEG5	130.01	140.33	158.16
HEAEPxPEG10	133.24	133.50	122.55
HEAEPxPEG20	134.47	132.33	91.93
HEMAEPyPEG0	120.27	137.17	237.23
HEMAEPyPEG5	117.91	130.35	192.28
HEMAEPyPEG10	118.88	131.47	182.05
HEMAEPyPEG20	121.75	132.31	124.01

HEMAEPyPEG materials, which is related to a decrease in the crosslinking density of the epoxy network caused by the presence of PEG. Furthermore, it is observed that the shape of the curve remains quite uniform, with similar values for the peaks, indicating that there is a homogeneous network structure, without separation between the acrylic and epoxy domains, which can be ascribed to the presence of the HEMA/HEA coupling agents, in a similar way to other 3D-printable dual systems [41]. The HEAEPxPEG system exhibits tan δ peaks at approximately 3 °C, 30 °C, 44 °C, and 55 °C for formulations containing 20, 10, 5, and 0 wt% of PEG. For HEMAEPyPEG systems, tan δ peaks are observed at 46 °C, 96 °C, 105 °C, and 154 °C, for formulations containing 20, 10, 5, and 0 wt% of PEG respectively. These shifts reflect the progressive impact of PEG content on the network structure. Table 4 presents the main mechanical properties of the formulations, including the crosslinking densities. Notably, the decrease in crosslinking density with increasing PEG content is consistent with the observed shift in tan δ peaks, confirming the plasticizing effect of PEG on the final network. The crosslinking density was calculated based on the rubber elasticity theory, as described in Equation (2):

$$\nu_e = \frac{E'}{3RT} \tag{2}$$

where ν_e is the crosslinking density expressed in moles per cubic meter

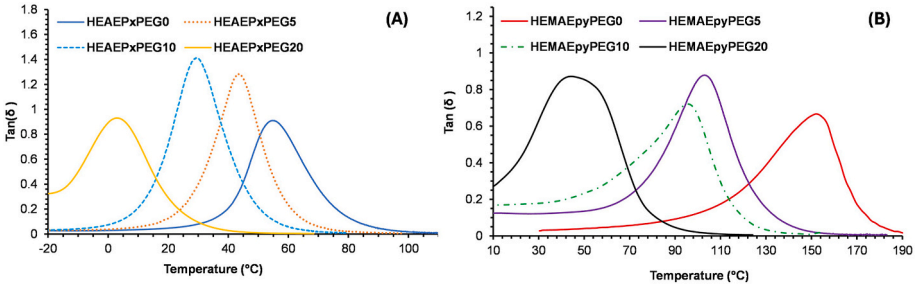

Fig. 3. Evaluation of the tan(δ) for all the formulations considered in both systems. (A) Evaluation of the tan(δ) for the system HEAEPxPEG. (B) Evaluation of the tan (δ) for the system HEMAEPyPEG.

Table 4
Glass transition temperature (Tg), rubbery plateau temperature (T rubbery), and rubbery elastic modulus (E′) used to calculate the crosslinking density (ν_e) via rubber elasticity theory.

Formulation	Tg (°C)	T rubbery (°C)	E' rubbery (MPa)	Cross-link densityg (mol/m^3)
HEAEPxPEG0	55.3	83	10.2	1146.7
HEAEPxPEG5	44.2	81	6.8	766.1
HEAEPxPEG10	30.0	73	4.7	538.6
HEAEPxPEG20	3.1	24	3.3	438.8
HEMAEPyPEG0	154.0	169	20.8	1890.9
HEMAEPyPEG5	105.0	139	9.2	895.2
HEMAEPyPEG10	96.0	138	5.4	527.1
HEMAEPyPEG20	46.0	93	3.6	396.1

(mol/m^3), E′ is the elastic modulus measured in Pascals (Pa) at a temperature T within the rubbery plateau region, R is the universal gas constant (8.314 J/mol), and T is the absolute temperature in Kelvin (K) at which E′ was determined.

These results evidence the possibility of tuning the final material properties depending on the combination of coupling agent, epoxy component, and PEG, leading to final materials with properties ranging from those of rigid solid, with high tan(δ) peaks around 150 °C, to very flexible materials with peaks near 0 °C. The remaining outputs of the dynamo mechanical analysis (E', E") can be found in Figures S-2 and Figures S-3 (see Supplementary Material).

Fig. 4 (A) shows the infrared spectra of formulations in solution of HEAEPxPEG0, HEAEPxPEG20, HEMAEPyPEG0, and HEMAEPyPEG20, showing slight differences in the shape of absorption bands. These differences can be attributed to the distinct chemical structure of the monomers used in each formulation. In particular, small variations are observed between the acrylate group in HEA-based formulations and the methacrylate group in HEMA-based ones, which affect the profile of the characteristic bands. A similar behavior is evident in the absorption bands corresponding to the epoxy monomers, where slight differences in band shape can be detected, likely due to structural and environmental differences between the formulations. However, the presence of PEG in the formulations does not result in significant changes in the infrared spectra. Fig. 4 (B) presents the infrared (IR) spectra corresponding to the formulations HEAEPxPEG20 in solution, at the intermediate stage, and at the final state. The bands between 16001650 cm^{-1}, 1410-1390 cm^{-1}, 1280-1310 cm^{-1} are used to analyze the reaction of acrylate/methacrylate groups [42], while the peak at 760-820 cm^{-1} is used to analyze the epoxy groups [43]. It is clearly seen that the acrylate/methacrylate groups disappear completely at the end of the 1st stage, while the epoxy groups remain unaltered. At the end of the 2nd stage, it can be observed that epoxy groups have also reacted completely. These results confirm the selective and controlled activation of the reactions taking place in the 1st and 2nd stages. On the other hand, Fig. 4 (C) presents the Raman spectra of MWCNTs-COOH, highlighting two prominent bands characteristic of these nanomaterials. The first band, known as the D-band, appears between 1260 and 1380 cm^{-1} and is associated with structural disorder in the carbon framework. The second, the G-band, located between 1520 and 1650 cm^{-1}, corresponds to the crystalline structure of

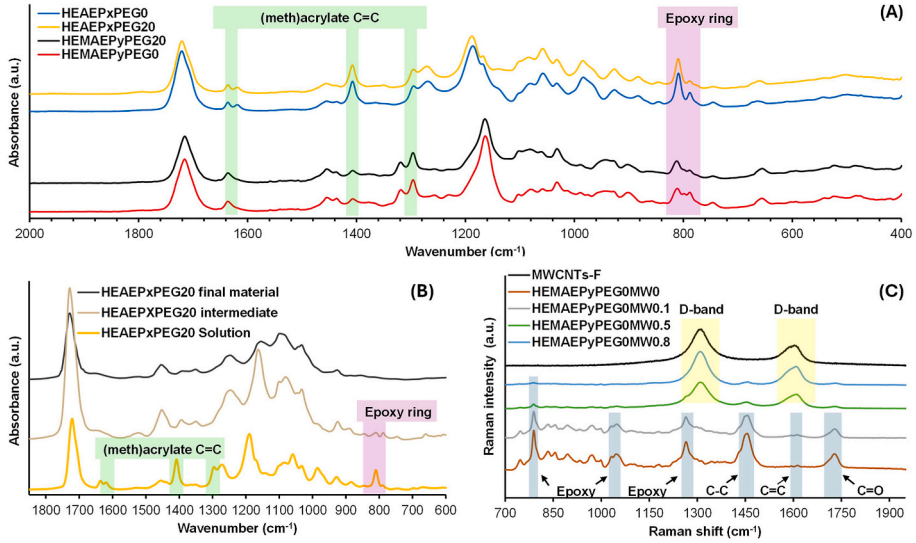

Fig. 4. Infrared spectra of formulations HEAEPxPEG0, HEAEPxPEG20, HEMAEPyPEG0, and HEMAEPyPEG20, showing slight differences in the shape of absorption bands (A). Infrared spectra analysis of HEMAEPyPEG20 in solution, intermediate, and final cured state (B). Raman spectra of HEMAEPyPEG0 formulations with varying MWCNTs-COOH concentrations (C).

sp^2-hybridized carbon atoms. The intensity ratio between these two bands I_D/I_G is a key indicator of the density of defects within the nanotubes, offering valuable insights into their structural integrity. In addition to the nanotubes, Fig. 4 (C) also illustrates the Raman spectra of the formulation HEMAEPyPEG0 in an intermediate state, with varying concentrations of MWCNTs-COOH. A notable trend emerges: as the concentration of nanotubes increases, the signals from other formulation components diminish. This behavior aligns with previous studies on composites incorporating MWCNTs, where increasing nanotube content influences the overall spectral profile [44]. The D- and G-bands remain prominent, alongside distinctive bands associated with the resin matrix. Further spectral analysis reveals key molecular bands characteristic of the formulation's components. A strong band near 1740 cm^{-1}, indicative of C═O bonds, is observed, along with a peak around 1450 cm^{-1}, corresponding to C–C bonds. These vibrations are prevalent in the main constituents of the formulation: the flexible acrylic resin, the coupling agent, and the epoxy resin. Notably, vibrations specific to the epoxy ring structure are also identified, with distinct bands appearing at 780, 833, 854, 1047, and 1265 cm^{-1}. These bands correspond to various molecular vibrations within the epoxy groups, offering insights into the intermediate state of the curing process. The identification of these molecular signatures provides a deeper understanding of the material's chemical composition and its evolving structure during the formulation's preparation [45]. Figure S-4 (see Supplementary Material) shows the full spectra of both formulations in solution, as well as in their intermediate and final states. Figure S-5 and Table S-1 (see Supplementary Material) show the spectra of the pristine MWCNTs and after the functionalization process, highlighting the bands associated with the newly formed bonds. Figure S-6 (see Supplementary Material) also provides a thermal DSC of the samples containing the amounts of MWCNTs for the formulation HEMAEPyPEG0.

Solubility test was conducted in dichlorobenzene to evaluate the gel content and swelling ratio in the PEG-containing formulations. The results of this analysis are presented in Table S2, showing the strong influence of the glass transition temperature (Tg) on the soluble fraction of systems. A greater mass loss was observed in networks with lower crosslinking density. This can be caused by both the occurrence of chain-transfer events with the participation of PEG, eventually leading to the formation of soluble, unbound epoxy polymer fragments, disturbing the epoxy-acrylic co-network structure, and by incomplete participation of excess PEG in the material, acting as plasticizer. The analysis of soluble fractions of high PEG samples in Figure S-7 suggest that the soluble fraction is composed mainly of PEG, but with a fraction of solubilized epoxy material, indicating that PEG can play both roles, but that a significant fraction of it is acting merely as plasticizer. In any case, this explains both the changes in thermal-mechanical properties discussed before, and will also have a relevant impact on the mechanical performance of the final materials.

3.2. Processing parameters

Viscosity is a critical parameter in 3D printing using VAT photopolymerization, as it directly influences the final properties of the material after the printing process. Additionally, printing times may depend on the viscosity of the solutions, due to the resin flow phenomena associated with the raising or lowering of the printing platform at each layer.

The apparent viscosity of each formulation, as detailed in Table 1, was precisely determined. As shown in Fig. 5 (A), a slight correlation is observed between the polyethylene glycol (PEG) content and viscosity, which consistently falls within the range of 15–35 mPa s. These values are influenced by the presence of coupling agents, HEMA and HEA, each comprising 40 wt% of the solutions. Notably, these methacrylates have relatively low nominal viscosities of 9 mPa s and 11.16 mPa s at 20 °C, respectively, which are significantly lower than those of the epoxy and acrylic components forming the base resin.

The results indicate that PEG modification does not substantially affect the viscosity of the liquid resin formulations, preserving their printability. When comparing both systems, the HEA-based formulation exhibits a higher viscosity, attributed to the intrinsic viscosity of the epoxy resin used in this system. Minor differences in viscosity are observed between the two formulations, but they remain within a comparable range. Additionally, a predominantly Newtonian behavior is evident across most of the analyzed shear rate range.

Furthermore, analysis of the Jacobs working curve reveals minimal discrepancies in processing. With minimal light exposure, uniform layer formation is achievable across all described systems, as demonstrated by the equal percentage of reagents activated by the printer's radiation for each formulation. Fig. 5 (B) provides an example comparing two different solutions with the same percentage of PEG. Figure S-8 shows all the Jacobs working curves for all the formulations. The analysis also indicates that the system using HEA as a coupling agent exhibits greater reactivity, resulting in thicker layers with similar exposure times. This outcome is expected, given that acrylates are more reactive than methacrylates, allowing for significant differences in resolution to be managed based on exposure time.

In the printing of the pieces, a layer resolution of 70 μm was used, ensuring excellent resolution. Fig. 5 (B) also shows the doses used to generate the 70-μm layers. It is evident that while 70-μm layers can be produced with lower doses, this configuration guarantees that they are sufficiently cross-linked to support themselves and be removed from the printer without compromising the quality of the piece. For each of the systems, values projected were double the selected layer dose, which was quite convenient for forming these pieces with good resolution while avoiding light scattering and minimizing undesired over-curing effects.

3.3. Mechanical characterization

The tensile analysis was conducted for each system to evaluate their mechanical behavior in both intermediate and final states. Special attention was given to the influence of PEG in both systems. Fig. 6 (A) shows the tensile stress graphs for the HEAEPxPEG formulation in their intermediate state, evidencing their high flexibility. The modulus of

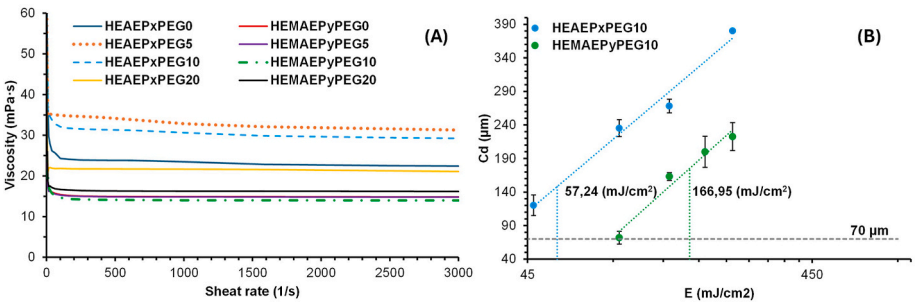

Fig. 5. Viscosity of both systems at 30 °C (A) and Jacobs' working curve for the formulations HEAEPxPEG5 and HEMAEPyPEG5 (B).

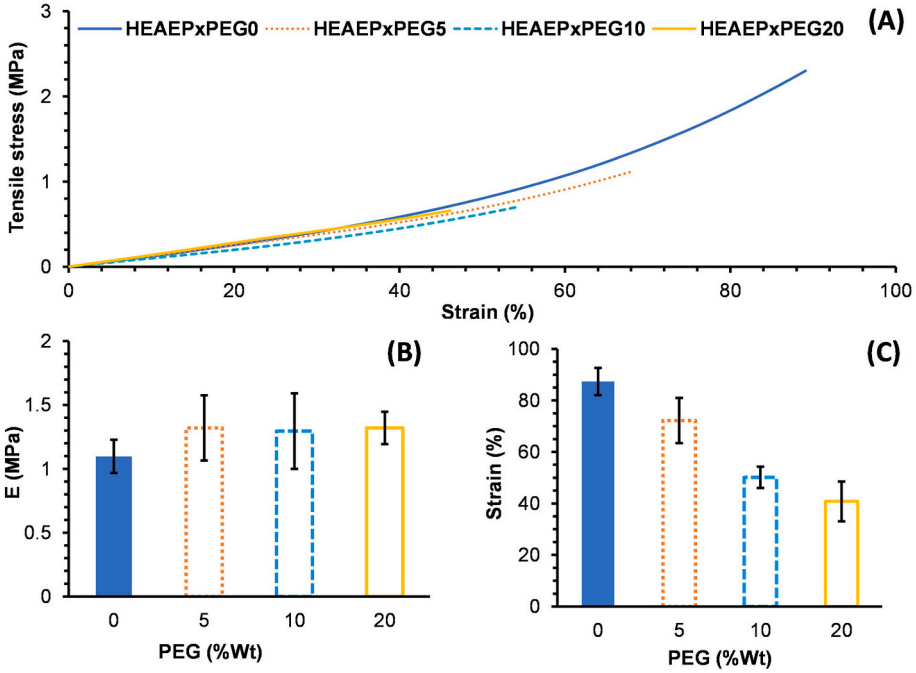

Fig. 6. Mechanical properties of HEAEPxPEG systems analyzed in the intermediate state. (A) HEAEPxPEG system, stress-strain behavior intermediate state, (B) HEAEPxPEG system, Young's modulus behavior intermediate state, (C) HEAEPxPEG system maximum strain behavior intermediate state.

elasticity is below 2 MPa for all the materials (see Fig. 6 (B)), and deformations up to 100 % can be achieved, decreasing with increasing PEG content, as seen in Fig. 6 (C).

In Fig. 7 (A), the behavior of the HEAEPxPEG formulations in their fully cured state is shown. A significant improvement in mechanical properties is evident, with increasing rigidity and maximum tensile stress compared to the intermediate state. Fig. 7 (B) shows the increase in the modulus of elasticity, which reaches values close to 1900 MPa with 0 % PEG content, while for the formulation containing 20 % PEG, this value drops to about 3 MPa. Furthermore, Fig. 7 (C) presents the strain values for each formulation, with maximum strain around 50 % and minimum close to 20 %. These values are clearly correlated with the glass transition temperature of the fully cured materials (see Fig. 3). The material with no PEG content has a tan(δ) peak somewhat higher than room temperature, leading to a rigid material but retaining a remarkable ductility. On increasing the PEG content, tan(δ) decreases the behavior of the material transitions to that of a rubbery material with lowest modulus for the material with lowest tan δ and higher PEG content. Signs of viscoelastic relaxation during the analysis are evident in the intermediate compositions, having a higher deformability for that reason [46]. The results of the mechanical analysis are summarized in Table 5.

The results of the analysis of the intermediate HEMAEPyPEG materials are shown in Fig. 8. The stress-strain curves in Fig. 8 (A) indicate that the intermediate materials are similar to those of the HEAEPxPEG systems but showing clearly higher deformability. Fig. 8 (B) indicates

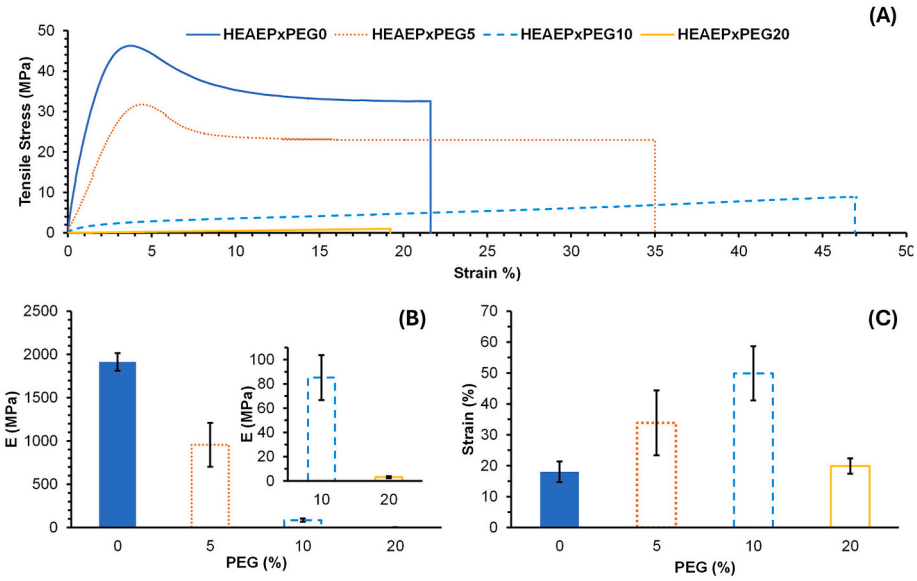

Fig. 7. Mechanical properties of HEAEPxPEG systems analyzed in the final state. (A) HEAEPxPEG system, stress-strain behavior the final state, (B) HEAEPxPEG system, Young's modulus behavior the final state, (C) HEAEPxPEG system maximum strain in the final state.

Table 5
Summary of principal mechanical properties of the HEAEPxPEG system.

Property	HEAEPxPEG0	HEAEPxPEG5	HEAEPxPEG10	HEAEPxPEG20
Max tensile stress (UV), MPa	1.51 ± 0.18	1.24 ± 0.17	0.74 ± 0.12	0.55 ± 0.01
E (UV), MPa	1.09 ± 0.13	1.32 ± 0.25	1.29 ± 0.29	1.32 ± 0.12
Strain (UV), %	87.34 ± 5.29	72.17 ± 8.75	50.10 ± 4.10	40.79 ± 7.46
Max tensile stress (UV-CC), MPa	44.78 ± 2.57	29.77 ± 2.99	9.29 ± 0.53	0.98 ± 0.15
E (UV-CC), MPa	1913.68 ± 101.43	955.60 ± 253.21	85.20 ± 18.46	3.18 ± 0.88
Strain (UV-CC), %	18.02 ± 3.32	33.85 ± 10.49	49.89 ± 8.73	19.89 ± 2.46

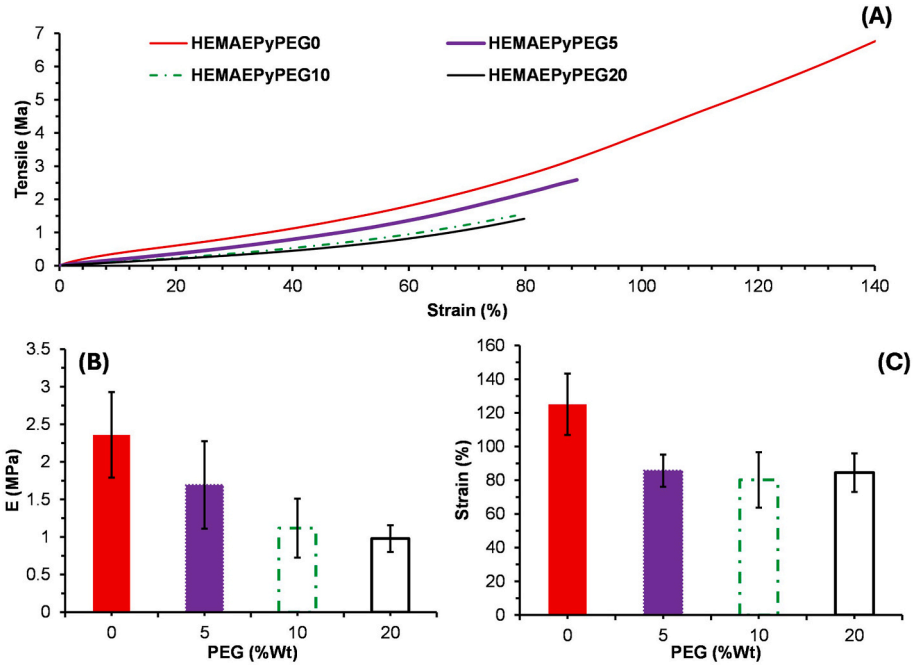

Fig. 8. Mechanical properties of HEMAEPyPEG systems analyzed in the intermediate state. (A) HEMAEPyPEG system, stress-strain behavior intermediate state; (B) HEMAEPyPEG system, Young's modulus behavior intermediate state; (C) HEMAEPyPEG system, Maximum strain behavior intermediate state.

that the values of the modulus of elasticity are low, remaining below 3 MPa for each formulation. Meanwhile, Fig. 8 (C) shows the deformation values, reaching maximums near 120 % and minimums around 80 %. The analysis of the mechanical behavior in the final state of the HEMAEPyPEG formulation reveals superior mechanical performance. Fig. 9 (A) illustrates drastic changes in mechanical behavior compared to the intermediate state, where a rigid behavior is evident in the stress-deformation graph. Fig. 9 (B) presents the modulus of elasticity values, reaching a maximum of 2500 MPa and a minimum close to 190 MPa, significantly higher than in the intermediate state. This is caused by the elevated glass transition temperature of these materials, as seen in Fig. 3, having tan(δ) peaks clearly higher than room temperature except for the material with the highest PEG content, with a tan(δ) peak around room temperature and evident signs of viscoelastic relaxation in the stress-strain behavior (see inset in Fig. 9 (A)). Finally, Fig. 9 (C) depicts the deformation values, showing a similarly radical outlook compared to the intermediate states, with maxima nearing 60 % and minima below 10 %.

Table 6 summarizes the principal mechanical properties in its intermediate and final state.

It is therefore quite apparent that PEG plays a significant role in both HEAEPxPEG and HEMAEPyPEG systems, with the only common components being the acrylic base and PEG content. However, differences in epoxy bases and coupling agents lead to distinct mechanical behaviors. The intermediate state consists of a solid with low crosslinking formed from the acrylic base and the coupling agent (HEA, HEMA). The mechanical properties depend on both the type of acrylic network formed, depending on the base acrylic resin and the coupling agent, as well as on the van der Waals interactions with the other components present in the system. Given that, at this stage, both unreacted epoxy and PEG would act as a plasticizer, the different mechanical behavior must be ascribed to the different role of HEA and HEMA in the radical polymerization process taking place in the 1st reaction stage. Methacrylates are known to undergo radical termination by a combination of disproportionation and combination reactions [47]. By way of contrast, acrylates are prone to undergo intra-molecular chain-transfer (back-biting) reactions [48, 49], which can lead to significant branching in polymer chains, producing faster gelation and shortening of network strands. This could be the reason why intermediate materials based on HEA are slightly different from HEMA intermediate states.

Upon completion of the thermal curing cycle, the final state is achieved, where epoxy networks crosslink with the coupling agent, resulting in a dense network primarily formed by covalent bonds and the growth of the epoxy resin. In the HEAEPxPEG system, ductile behavior is expected in the intermediate state, with a modest increase in mechanical properties in the final state. After thermal treatment, the HEAEPxPEG system shows enhanced mechanical properties due to the long-chain epoxy resin, resulting in less dense and more flexible co-networks. Conversely, the HEMAEPyPEG system features a short-chain epoxy resin and a methacrylate as the coupling agent. This system exhibits flexible behavior in its intermediate state but demonstrates better mechanical performance in terms of deformation. The methacrylate coupling agent enhances intermolecular interactions among the network components (epoxy/PEG). In its final state, the combination of the rigid methacrylate chain of HEMA with the short-chain epoxy resin EPy

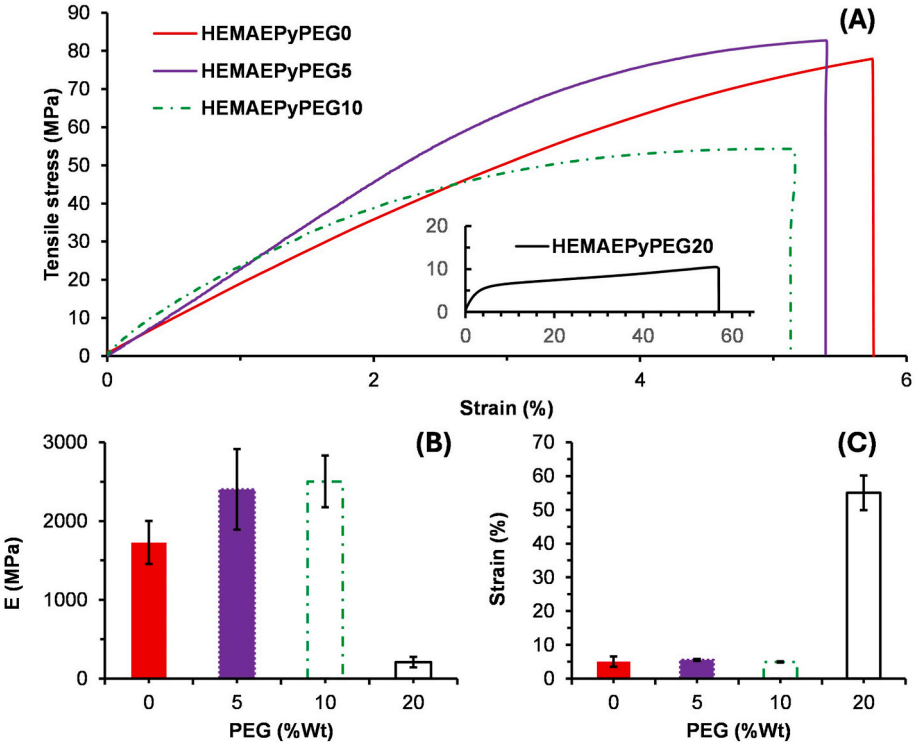

Fig. 9. Mechanical properties of HEMAEPyPEG systems analyzed in the final state. (A) HEMAEPyPEG system, stress-strain behavior in the final state, (B) HEMAEPyPEG system, young modulus behavior in the final state, (C) HEMAEPyPEG system Max strain behavior in the final state.

Table 6
Summary of principal mechanical properties of the HEMAEPyPEG system.

Property	HEMAEPyPEG0	HEMAEPYPEG5	HEMAEPYPEG10	HEMAEPYPEG20
Max tensile stress (UV), MPa	6.25 ± 0.57	2.46 ± 0.58	1.50 ± 0.39	1.45 ± 0.17
E (UV), MPa	2.36 ± 0.40	1.69 ± 0.31	1.11 ± 0.052	0.97 ± 0.03
Strain (UV), %	125.07 ± 18.20	85.68 ± 9.48	80.22 ± 16.43	84.50 ± 11.43
Max tensile stress (UV-CC), MPa	73.62 ± 6.12	81.17 ± 2.66	56.92 ± 3.67	8.15 ± 1.83
E (UV-CC), MPa	1278 ± 274	2053 ± 167	2503 ± 328	190.84 ± 74.74
Strain (UV-CC), %	5.06 ± 1.52	5.52 ± 0.30	4.93 ± 0.19	55.06 ± 5.12

contributes to a denser, more crosslinked network, resulting in a rigid material with improved structural capabilities. The presence of PEG in both networks allows the fine-tuning of the final material properties due to its effect as chain-transfer agent, therefore loosening the network structure, as well as plasticizer, resulting in a decrease in Tg.

3.4. Dual curing processing capabilities

One of the main advantages of 3D printing via vat photopolymerization, using the dual curing methodology, is the ability to produce parts with excellent resolution. Fig. 10 (A) shows the precision of the material in its intermediate state when printing a part with very small holes. Fig. 10 (B) highlights the flexibility of the material in its intermediate state, while Fig. 10 (C) illustrates its rigidity in the final, fully cured state. Additionally, a significant advantage is the possibility of post-processing after printing. Fig. 10 (D, E−1, E−2, F) presents examples where once printed, the parts can be modified to assume more complex geometries, which would otherwise require intricate printing configurations and considerably more time to produce. In Fig. 10 (D), it is shown how a highly malleable, perforated plate was successfully printed. In Fig. 10 (E−1), it is demonstrated that, due to the geometric versatility of the piece, it was possible to alter its shape. By using the same solution, two complementary pieces were printed to act as plugs. As seen in Fig. 10 (E−2), when joined, the material remained very flexible, capable of withstanding significant deformations. On the other hand, Fig. 10 (F) analyzes the piece in its final state, where it becomes rigid and supports loads in compression, providing a comparative view. This highlights the importance of the dual-curing strategy, as well as the versatility and characterization of the material in its intermediate state, and the importance of characterizing the joints.

Beyond these benefits, this methodology allows for the design of materials in their intermediate state, forming low-density, flexible networks capable of withstanding large deformations. This is particularly interesting because, with this approach, it is possible to create large parts without the size being limited by the maximum deformations the parts can withstand during the layer formation process in printing. Materials can be designed to handle deformations exceeding 60 %, which is much higher than the deformations caused by shrinkage or swelling.

At the same time, this dual-curing approach also allows for control over the mechanical properties of the material in its final state, enabling the design of materials for structural applications with strengths exceeding 80 MPa. Additionally, the incorporation of PEG has shown that the networks can be tailored to meet the desired mechanical properties from a rigid to a flexible and soft material. This is a highly effective strategy for two main reasons. First, the solutions exhibit low viscosities due to the use of low molecular weight components participating in the 1st and 2nd curing stages, which is crucial for reducing

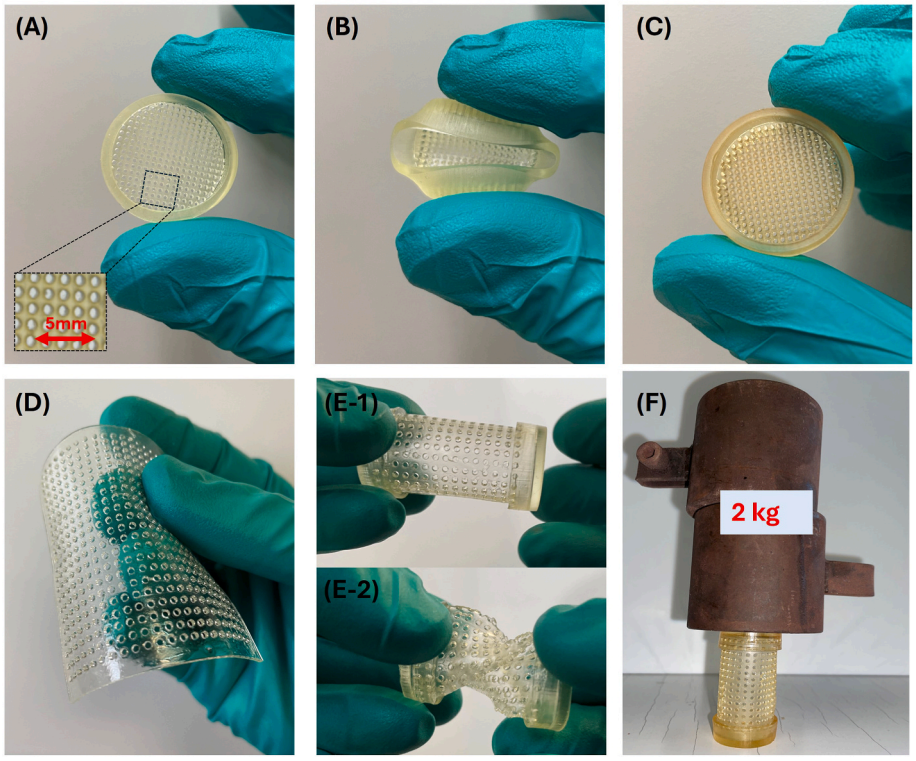

Fig. 10. (A) Part printed with high resolution, (B) sample shows high flexibility and high deformation stability, (C) rigid material after thermal treatment. (D) Printed flexible sheet with holes, (E−1) cylinder-shaped sheet and joint with two printed covers of the same flexible material, (E−2) glued and folded piece. (F) Piece after heat treatment showing its ability to withstand loads without deforming.

processing times. Second, a wide range of final mechanical properties can be reached, without affecting the viscosity of the formulation, as can be seen in Fig. 11, where the results of the present system are compared with a survey of literature values. The key point is that this is accomplished by just changing a few components in the formulation, without altering the design concept: a base crosslinking acrylic resin combined with an acrylic/methacrylic chain-extender that acts as coupling agent, an epoxy component, and a polyol chain extender.

From the perspective of assembly and bonding of printed parts, the controlled dual-curing strategy offers several advantages. It allows for mechanical bonding in two steps: first, ultraviolet light can be used to rapidly activate the resin in its intermediate state, enabling bonding of

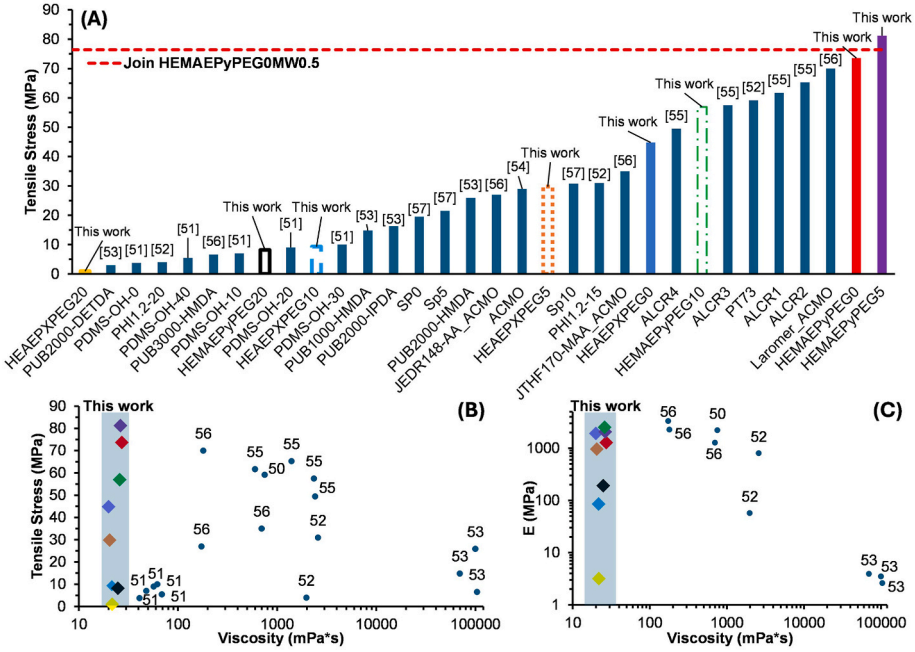

Fig. 11. (A) Comparison of maximum tensile stress in various systems reported in the literature, (B) comparison between tensile stress and viscosity in various systems reported in the literature, (C) comparison of elastic modulus and viscosity reported in the literature [50–57].

the parts with just light exposure on the surface. This allows for quick inspection to ensure that the entire surface has been properly bonded. Fig. 12 (A) provides a comparison of different solutions applied to the bonding of components under structural demands, with the HEMAE-PyPEG solution in its bulk state serving as a reference. The continuous red line represents the maximum tensile strength in this bulk state. The performance of the bonds is depicted in the bars, where it can be observed that the sample without filler exhibits acceptable tensile strength, though it falls short of the bulk material's average. By examining the values obtained for the HEMAEPyPEG0 adhesive in its final state, it becomes evident that the dual-curing strategy activates the residual acrylic and epoxy groups in both the solution and the partially activated solid in a controlled and sequential manner. This process generates covalent bonds at the interfaces of the bonded parts, resulting in a densely crosslinked network with excellent adhesive properties when the solution is used as an adhesive. The results of this approach yielded maximum tensile strength values of 65 MPa, representing 87 % of the bulk material's strength, as can be seen in Fig. 12 (A) with the code 0 %MW HEMA. While the same solution shows promising results, the bond strength is insufficient to endure the same stresses as the bulk material.

Further enhancement of mechanical and adhesive properties was achieved by incorporating MWCNTs-COOH into the solution. When combined with a standardized joining protocol and proper dispersion of the MWCNTs-COOH, a dual-curing nanoadhesive can be developed.

The explanation for the observed improvement in adhesive performance is based on reinforcement mechanisms well established in the literature on carbon nanotubes and their effects in polymer matrices. In particular, the high specific surface area of MWCNTs promotes efficient load transfer between bonded parts, enabling a more uniform distribution of mechanical stresses across the adhesive interface, thereby reducing localized stress concentrations that could lead to premature failure [58,59]. Additionally, the three-dimensional dispersion of the nanotubes acts as a physical barrier against microcrack propagation, enhancing fracture resistance under load. This effect is linked to well-documented mechanisms such as plastic deformation of the polymer matrix, crack deflection around nanotube agglomerates, and crack bridging by the nanotubes themselves, which delay crack growth and increase the energy absorbed prior to failure [60], thereby improving the mechanical and adhesive strength of the bonded interfaces.

Furthermore, the carboxyl (-COOH) group plays a pivotal role in improving the dispersion of the nanofiller and enables the controlled participation in the sequential activation of curing reactions. This ensures that the base formulation preserves its inherent advantages while gaining enhanced mechanical and adhesive performance from the well-dispersed MWCNTs-COOH. As can be seen in Fig. 12(A) the incorporation of multi-walled carbon nanotubes (MWCNTs) into the adhesive solution leads to a marked increase in tensile strength, attributed to their excellent dispersion and inherent properties. At a concentration of 0.1 % MWCNTs, tensile strength values approach those of the bulk material. Increasing the concentration to 0.5 % brings the values in line with the bulk material's average, indicating proper dispersion and strong phase interaction that enhances both the bond's strength and adhesion between the substrate and the adhesive. Representative images of bonded two-dimensional structures are included in the Supplementary Information (Figure S-9 (A)), illustrating the potential of the adhesive formulation to effectively connect printed parts. Moreover, additional observations were carried out to evaluate the dispersion stability of MWCNTs-COOH within the adhesive formulation. As part of this study, photographs were taken immediately after preparation, and after 1 h, 2 h, 8 h, 1 day, 1 week, and 2 weeks of rest. These images, provided in the Supplementary Information (Figure S-9 (B)) and at a higher concentration of 0.8 % MWCNTs, however, tensile strength decreases significantly, a result attributed to poor nanomaterial dispersion, which concentrates stress in a stiffer and less uniform matrix. Fig. 12 (B) illustrates this interaction between the two phases, highlighting how covalent bonding between the nanoadhesive and the printed solid parts significantly enhances the adhesive matrix. The COOH group not only facilitates dispersion, increasing the chemical compatibility, but also actively participates in the epoxy resin's ring-opening reaction, promoting the formation of covalent bonds. This reaction has been reported in the literature and typically involves the formation of ester (CO–O–C) linkages between the –COOH groups on the MWCNTs and the epoxide [61–63], which reinforces adhesion by creating stronger interactions between the adhesive and the substrate, while the residual groups present in the printed parts will also participate in the bonding with the nanotubes, enhancing their adhesion capabilities as well as improving the overall interaction of the joint. On the other hand, the joint strength was analyzed using parts printed with the HEAEPxPEG0 formulation. These parts were bonded using two types of adhesives: HEAEPxPEG0, as a self-adhesive, and HEMAEPyPEG0, as an alternative high-strength adhesive. The results showed that the adhesive capacity of HEAEPxPEG0 did not reach the performance of the material in its bulk state. This could be explained by the differences in the nature of the epoxy resins used: while the epoxy resin in the HEMA system provides greater stiffness and mechanical strength in the final state, the epoxy resin in the HEA system exhibits lower mechanical performance, which may limit its adhesive capacity. As shown in Fig. 12, the blue line represents the performance of the material in its bulk state, and although the joints made with HEAEPxPEG0 demonstrate acceptable strength, they fall short of matching the performance of the bulk material.

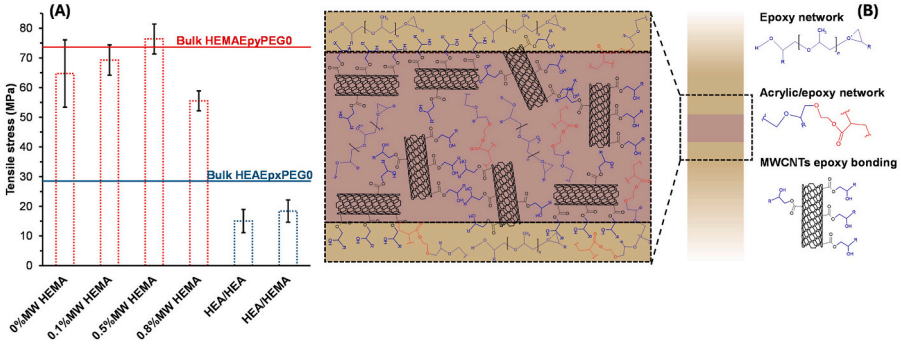

Fig. 12. (A) The solid red and blue lines represent the results obtained for the HEMAEPyPEG0 and HEAEPxPEG0 formulations, respectively, in fully printed and bulk-cured parts. For the red dashed lines, different variants of the HEMAEPyPEG0 formulation were analyzed as adhesives: one without nanotubes and others with concentrations of 0.1 %, 0.5 %, and 0.8 % of MWCNTs-COOH. For the blue dashed lines, the HEAEPxPEG0 and HEMAEPyPEG0 formulations were used as adhesives. (B) Representative diagram of how nanotubes can participate and enhance the mechanical properties of the joints. (For interpretation of the references to colour in this figure legend, the reader is referred to the Web version of this article.)

4. Conclusion

This study has demonstrated the effectiveness of an innovative strategy based on dual curing in Vat 3D photopolymerization, allowing the creation of crosslinked networks with adjustable mechanical properties in acrylic/epoxy systems. The control of crosslinking and spatial occupation within the material has been crucial in modifying the final mechanical properties without compromising processing ease. This methodology offers significant advantages both in fabrication and post-processing, providing greater flexibility in the design of complex parts. A key aspect of this work is the inclusion of PEG as a chain extender, which played a fundamental role by reacting its –OH groups with the growing epoxy resin, covalently bonding the existing networks, as well as a plasticizer with excellent compatibility with the matrix. To study the influence of PEG on the crosslinking of the networks, concentrations of 20 wt%, 10 wt%, and 5 wt% were evaluated in both acrylic/epoxy systems. The results showed that increasing amount of PEG led to lower crosslinking and Tg, having a significant impact on thermal and mechanical properties. This approach made it possible to prepare materials with a wide range of Tg varying between 150 °C and 0 °C depending on the composition. The tensile strengths obtained, ranging between 1 MPa and 80 MPa, highlight the system's ability to adjust and optimize the networks according to the specific requirements of each application. Additionally, the solutions exhibited a low viscosity in the range of 15–35 mPa s, considerably lower than that reported in the literature. Despite these lower viscosities, no negative influence was observed on the final mechanical properties. The tolerance to deformation of up to 125 % in the intermediate state is crucial for shaping large parts without compromising structural stability during processing. Moreover, this work also emphasizes the use of novel tensile testing on bonded joints, offering a more accurate evaluation of mechanical behavior in complex structures. The results show that the HEMAEPyPEG0 system achieved up to 80 % of the tensile strength compared to the bulk state, confirming the excellent adhesive capacity of the systems evaluated. Finally, the inclusion of MWCNTs-COOH as reinforcement improved the adhesive and mechanical properties of the system, generating additional covalent bonds between the adherent and adhesive phases. This nano-adhesive approach offers considerable potential for future applications in 3D printing, especially in cases where durability and mechanical strength are key aspects.

CRediT authorship contribution statement

A.A. Escriba-Flores: Writing – original draft, Visualization, Validation, Investigation, Formal analysis. **X. Fernández-Francos:** Writing – review & editing, Supervision, Resources, Project administration, Methodology, Conceptualization. **F. Ferrando:** Supervision, Conceptualization. **A. Fabregat-Sanjuan:** Writing – review & editing, Supervision, Resources, Methodology, Conceptualization.

Declaration of competing interest

The authors declare the following financial interests/personal relationships which may be considered as potential competing interests:A. A. Escriba-Flores has patent #U 202431191 pending to Universitat Rovira i Virgili. X. Fernandez-Francos has patent #U 202431191 pending to Universitat Politècnica de Catalunya. A. Fabregat-Sanjuan has patent #U 202431191 pending to Universitat Rovira i Virgili. If there are other authors, they declare that they have no known competing financial interests or personal relationships that could have appeared to influence the work reported in this paper.

Acknowledgements

This work was funded by the Spanish Ministry of Science and Innovation (MCIN/AEI/10.13039/501100011033) through R&D projects PID2020-115102RB-C21, PID2020-115102RB-C22 and PID2023-147128OB-C21, and also by Generalitat de Catalunya (2021-SGR-154). Armando Escribá acknowledges to the Martí Franqués fellowship program (2021PMF-BS-08). X. Fernández-Francos acknowledges the Serra-Húnter programme (Generalitat de Catalunya).

Appendix A. Supplementary data

Supplementary data to this article can be found online at https://doi.org/10.1016/j.polymer.2025.128768.

Data availability

Data will be made available on request.

References

[1] W. Gao, Y. Guo, J. Cui, C. Liang, Z. Lu, S. Feng, Y. Sun, Q. Xia, B. Zhang, Dual-curing polymer systems for photo-curing 3D printing, Addit. Manuf. 85 (2024) 104142, https://doi.org/10.1016/j.addma.2024.104142.
[2] J. Cao, K. Miao, S. Xiong, F. Su, D. Gao, X. Lin, Z. Liu, P. Wang, C. Liu, Z. Chen, 3D printing and in situ transformation of SiCnw/SiC structures, Addit. Manuf. 58 (2022) 103053, https://doi.org/10.1016/j.addma.2022.103053.
[3] Y. Lu, X. Han, A. Gleadall, F. Chen, W. Zhu, L. Zhao, Continuous fibre reinforced vat photopolymerisation (CONFIB-VAT), Addit. Manuf. 60 (2022) 103233, https://doi.org/10.1016/j.addma.2022.103233.
[4] S.V. Smirnov, P.V. Protsenko, M.A. Goldberg, T.O. Obolkina, O.S. Antonova, K. V. Malyutin, G.P. Kochanov, A.A. Konovalov, YuM. Nevolin, A.V. Volkov, S. A. Akhmedova, V.A. Kirsanova, I.K. Sviridova, N.S. Sergeeva, S.M. Barinov, V. M. Ievlev, V.S. Komlev, Vat photopolymerization 3D printing of yttria-stabilized ZrO_2 ceramics: effects of a sintering additive (Na_2O – $2SiO_2$), biocompatibility, and osteointegration, Addit. Manuf. 84 (2024) 104071, https://doi.org/10.1016/j.addma.2024.104071.
[5] S. Kim, E.-H. Kim, W. Lee, M. Sim, I. Kim, J. Noh, J.-H. Kim, S. Lee, I. Park, P.-C. Su, A. Andreu, Y.-J. Yoon, Real-time in-process control methods of process parameters for additive manufacturing, J. Manuf. Syst. 74 (2024) 1067–1090, https://doi.org/10.1016/j.jmsy.2024.05.008.
[6] S. Lee, Y. Kim, D. Park, J. Kim, The thermal properties of a UV curable acrylate composite prepared by digital light processing 3D printing, Compos. Commun. 26 (2021) 100796, https://doi.org/10.1016/j.coco.2021.100796.
[7] S. Keck, O. Liske, K. Seidler, B. Steyrer, C. Gorsche, S. Knaus, S. Baudis, Synthesis of a liquid lignin-based methacrylate resin and its application in 3D printing without any reactive diluents, Biomacromolecules 24 (2023) 1751–1762, https://doi.org/10.1021/acs.biomac.2c01505.
[8] X. Yao, X. Yang, Y. Lu, R. Wang, Y. Guo, X. Jia, Vat photopolymerization 3D printing engineering plastics, in: Vat Photopolymerization Additive Manufacturing, Elsevier, 2024, pp. 77–118, https://doi.org/10.1016/B978-0-443-15487-4.00006-6.
[9] A. Al Rashid, W. Ahmed, M.Y. Khalid, M. Koç, Vat photopolymerization of polymers and polymer composites: processes and applications, Addit. Manuf. 47 (2021) 102279, https://doi.org/10.1016/j.addma.2021.102279.
[10] M. Pagac, J. Hajnys, Q.P. Ma, L. Jancar, J. Jansa, P. Stefek, J. Mesicek, A review of vat photopolymerization technology: materials, applications, challenges, and future trends of 3d printing, Polymers 13 (2021) 1–20, https://doi.org/10.3390/polym13040598.
[11] L.J. Tan, W. Zhu, K. Zhou, Recent progress on polymer materials for additive manufacturing, Adv. Funct. Mater. 30 (2020) 2003062, https://doi.org/10.1002/adfm.202003062.
[12] H. Wang, Z. Huang, Y. Zhang, L. Li, J. Li, Design of enhanced mechanical properties by interpenetrating network of 3D printing dual-curing resins, Polymer (Guildf.) 282 (2023) 126153, https://doi.org/10.1016/j.polymer.2023.126153.
[13] Y. Huang, X. Gao, Y. Zhang, B. Ma, Laser joining technology of polymer-metal hybrid structures - a review, J. Manuf. Process. 79 (2022) 934–961, https://doi.org/10.1016/j.jmapro.2022.05.026.
[14] M. Devine, A. Bajpai, C.M. Ó Brádaigh, D. Ray, 'Resin welding': a novel route to joining acrylic composite components at room temperature, Compos. B Eng. 272 (2024) 111212, https://doi.org/10.1016/j.compositesb.2024.111212.
[15] X. Yu, Z. Wang, Z. Yu, Y. Wang, K. Zhong, Y. Zhao, J. Zhao, Additive manufacturing and joining double processes of ceramic-resin green bodies using a single- or double-phase photocuring slurry, Ceram. Int. 50 (2024) 14088–14100, https://doi.org/10.1016/j.ceramint.2024.01.292.
[16] M.R. Khosravani, P. Soltani, T. Reinicke, Fracture and structural performance of adhesively bonded 3D-printed PETG single lap joints under different printing parameters, Theor. Appl. Fract. Mech. 116 (2021), https://doi.org/10.1016/j.tafmec.2021.103087.
[17] M.R. Khosravani, P. Soltani, T. Reinicke, Failure and fracture in adhesively bonded 3D-printed joints: an overview on the current trends, Eng. Fail. Anal. 153 (2023), https://doi.org/10.1016/j.engfailanal.2023.107574.
[18] V. Dahmen, A.J. Redmann, J. Austermann, A.L. Quintanilla, S.J. Mecham, T. A. Osswald, Fabrication of hybrid composite T-joints by co-curing with 3D printed

dual cure epoxy, Compos. B Eng. 183 (2020) 107728, https://doi.org/10.1016/j.compositesb.2019.107728.
[19] A. Roig, X. Ramis, S. De la Flor, À. Serra, Dual-cured thermosets based on eugenol derivatives and thiol chemistry, Eur. Polym. J. 200 (2023) 112499, https://doi.org/10.1016/j.eurpolymj.2023.112499.
[20] X. Ramis, X. Fernández-Francos, S. De la Flor, F. Ferrando, À. Serra, Click-based dual-curing thermosets and their applications, in: Thermosets, Elsevier, 2018, pp. 511–541, https://doi.org/10.1016/B978-0-08-101021-1.00016-2.
[21] O. Konuray, J.M. Morancho, X. Fernández-Francos, M. García-Alvarez, X. Ramis, Curing kinetics of dually-processed acrylate-epoxy 3D printing resins, Thermochim. Acta 701 (2021) 178963, https://doi.org/10.1016/j.tca.2021.178963.
[22] X. Fernández-Francos, O. Konuray, X. Ramis, À. Serra, S. De la Flor, Enhancement of 3D-printable materials by dual-curing procedures, Materials 14 (2021) 1–23, https://doi.org/10.3390/ma14010107.
[23] W. Wu, H. Feng, L. Xie, A. Zhang, F. Liu, Z. Liu, N. Zheng, T. Xie, Reprocessable and ultratough epoxy thermosetting plastic, Nat. Sustain. 7 (2024) 804–811, https://doi.org/10.1038/s41893-024-01331-9.
[24] Y. Du, D. Wang, One-pot preparation of double-network epoxy vitrimers with high performance, recyclability, and two-stage stress relaxation, ACS Appl. Mater. Interfaces 16 (2024) 41551–41561, https://doi.org/10.1021/acsami.4c09123.
[25] O. Konuray, A. Sola, J. Bonada, A. Tercjak, A. Fabregat-Sanjuan, X. Fernández-Francos, X. Ramis, Cost-effectively 3D-Printed rigid and versatile interpenetrating polymer networks, Materials 14 (2021) 4544, https://doi.org/10.3390/ma14164544.
[26] A. Vilanova-Pérez, S. De la Flor, X. Fernández-Francos, À. Serra, A. Roig, Biobased imine vitrimers obtained by photo and thermal curing procedures—promising materials for 3D printing, ACS Appl. Polym. Mater. (2023), https://doi.org/10.1021/acsapm.3c03234.
[27] J.W. Kopatz, J. Unangst, A.W. Cook, L.N. Appelhans, Compositional effects on cure kinetics, mechanical properties and printability of dual-cure epoxy/acrylate resins for DIW additive manufacturing, Addit. Manuf. 46 (2021) 102159, https://doi.org/10.1016/j.addma.2021.102159.
[28] Y. Wei, X. Jin, Q. Luo, Q. Li, G. Sun, Adhesively bonded joints – a review on design, manufacturing, experiments, modeling and challenges, Compos. B Eng. 276 (2024), https://doi.org/10.1016/j.compositesb.2024.111225.
[29] P.K. Tyagi, R. Kumar, Z. Said, Recent advances on the role of nanomaterials for improving the performance of photovoltaic thermal systems: trends, challenges and prospective, Nano Energy 93 (2022), https://doi.org/10.1016/j.nanoen.2021.106834.
[30] J. Lu, Y. Fu, Y. He, K. Zheng, F. Sun, J. Zhang, X. Cao, Y. Ma, Enhancing thermal conductance between graphene and epoxy interfaces through non-covalent cation-π interactions, Carbon N Y 226 (2024), https://doi.org/10.1016/j.carbon.2024.119236.
[31] S. Liu, V.S. Chevali, Z. Xu, D. Hui, H. Wang, A review of extending performance of epoxy resins using carbon nanomaterials, Compos. B Eng. 136 (2018) 197–214, https://doi.org/10.1016/j.compositesb.2017.08.020.
[32] M. Al-Zu'bi, L. Anguilano, M. Fan, Effect of incorporating carbon- and silicon-based nanomaterials on the physico-chemical properties of a structural epoxy adhesive, Polym. Test. 128 (2023), https://doi.org/10.1016/j.polymertesting.2023.108221.
[33] Y. Korkmaz, K. Gültekin, Effect of UV irradiation on epoxy adhesives and adhesively bonded joints reinforced with BN and B4C nanoparticles, Polym. Degrad. Stabil. 202 (2022), https://doi.org/10.1016/j.polymdegradstab.2022.110004.
[34] U.A. Khashaba, A.A. Aljinaidi, M.A. Hamed, Fatigue and reliability analysis of nano-modified scarf adhesive joints in carbon fiber composites, Compos. B Eng. 120 (2017) 103–117, https://doi.org/10.1016/j.compositesb.2017.04.001.
[35] A.A. Escriba-Flores, X. Fernández-Francos, F. Ferrando, A. Fabregat-Sanjuan, Evaluation of the effect of coupling agent on the kinetic and mechanical properties of a 3D printable dual curing epoxy/acrylate system, Eur. Polym. J. 229 (2025) 113878, https://doi.org/10.1016/j.eurpolymj.2025.113878.
[36] H. Mozaffarinasab, M. Jamshidi, Synthesis of highly grafted MWCNTs with epoxy silane to improve curing, thermal and mechanical performances of epoxy nanocomposites, Diam. Relat. Mater. 141 (2024) 110668, https://doi.org/10.1016/j.diamond.2023.110668.
[37] Z. Chen, J. Luo, Z. Huang, C. Cai, R. Tusiime, Z. Li, H. Wang, C. Cheng, Y. Liu, Z. Sun, H. Zhang, J. Yu, Synergistic toughen epoxy resin by incorporation of polyetherimide and amino groups grafted MWCNTs, Compos. Commun. 21 (2020) 100377, https://doi.org/10.1016/j.coco.2020.100377.
[38] M.N. Siddiqui, D.S. Achilias, H.H. Redhwi, Effect of the side ethylene glycol and hydroxyl groups on the polymerization kinetics of oligo(ethylene glycol methacrylates). An experimental and modeling investigation, Polym. Chem. 11 (2020) 3732–3746, https://doi.org/10.1039/D0PY00498G.
[39] O. Konuray, F. Di Donato, M. Sangermano, J. Bonada, A. Tercjak, X. Fernandez-Francos, A. Serra, X. Ramis, Dual-curable stereolithography resins for superior thermomechanical properties, Express Polym. Lett. 14 (2020) 881–894, https://doi.org/10.3144/expresspolymlett.2020.72.
[40] J.V. Crivello, U. Varlemann, Structure and reactivity relationships in the photoinitiated cationic polymerization of 3,4-Epoxycyclohexylmethyl-3′,4′-epoxycyclohexane carboxylate, 82–94, https://doi.org/10.1021/bk-1997-0673.ch007, 1997.
[41] O. Konuray, A. Sola, J. Bonada, A. Tercjak, A. Fabregat-Sanjuan, X. Fernández-Francos, X. Ramis, Cost-effectively 3D-Printed rigid and versatile interpenetrating polymer networks, Materials 14 (2021) 4544, https://doi.org/10.3390/ma14164544.
[42] A.O. Konuray, A. Ruiz, J.M. Morancho, J.M. Salla, X. Fernández-Francos, À. Serra, X. Ramis, Sequential dual curing by selective michael addition and free radical polymerization of acetoacetate-acrylate-methacrylate mixtures, Eur. Polym. J. 98 (2018) 39–46, https://doi.org/10.1016/j.eurpolymj.2017.11.003.
[43] X. Fernàndez-Francos, S.G. Kazarian, X. Ramis, À. Serra, Simultaneous monitoring of curing shrinkage and degree of cure of thermosets by attenuated total reflection fourier transform infrared (ATR FT-IR) spectroscopy, Appl. Spectrosc. 67 (2013) 1427–1436, https://doi.org/10.1366/13-07169.
[44] A.L. Kaiser, I.V. Albelo, B.L. Wardle, Fabrication of aerospace-grade epoxy and bismaleimide matrix nanocomposites with high density aligned carbon nanotube reinforcement, in: AIAA Scitech 2020 Forum, American Institute of Aeronautics and Astronautics, Reston, Virginia, 2020, https://doi.org/10.2514/6.2020-2256.
[45] A.P. Kotula, J.W. Woodcock, J.W. Gilman, G.A. Holmes, A cure kinetics investigation of amine-cured epoxy by rheo-raman spectroscopy, Elsevier Ltd, https://doi.org/10.1016/j.polymer.2023.125967, 2023.
[46] A. Belmonte, G.C. Lama, G. Gentile, P. Cerruti, V. Ambrogi, X. Fernández-Francos, S. De la Flor, Thermally-triggered free-standing shape-memory actuators, Eur. Polym. J. 97 (2017) 241–252, https://doi.org/10.1016/j.eurpolymj.2017.10.006.
[47] Y. Nakamura, S. Yamago, Termination mechanism in the radical polymerization of methyl methacrylate and styrene determined by the reaction of structurally well-defined polymer end radicals, Macromolecules 48 (2015) 6450–6456, https://doi.org/10.1021/acs.macromol.5b01532.
[48] N. Ballard, S. Hamzehlou, F. Ruipérez, J.M. Asua, On the termination mechanism in the radical polymerization of acrylates, Macromol. Rapid Commun. 37 (2016) 1364–1368, https://doi.org/10.1002/marc.201600278.
[49] T. Pirman, M. Ocepek, B. Likozar, Radical polymerization of acrylates, methacrylates, and styrene: biobased approaches, mechanism, kinetics, secondary reactions, and modeling, Ind. Eng. Chem. Res. 60 (2021) 9347–9367, https://doi.org/10.1021/acs.iecr.1c01649.
[50] Z. Chen, M. Yang, M. Ji, X. Kuang, H.J. Qi, T. Wang, Recyclable thermosetting polymers for digital light processing 3D printing, Mater. Des. 197 (2021) 109189, https://doi.org/10.1016/j.matdes.2020.109189.
[51] D. Wang, R. Wang, S. Chen, J. Gao, C. Cai, Y. Zheng, X. Liu, B. Qu, N. Chen, D. Zhuo, Low viscosity and highly flexible stereolithographic 3D printing resins for flexible sensors, Mater. Des. 243 (2024) 113052, https://doi.org/10.1016/j.matdes.2024.113052.
[52] W. Huang, Z. Zu, Y. Huang, H. Xiang, X. Liu, UV-curing 3D printing of high-performance, recyclable, biobased photosensitive resin enabled by dual-crosslinking networks, Addit. Manuf. 91 (2024) 104352, https://doi.org/10.1016/j.addma.2024.104352.
[53] X. Huang, S. Peng, L. Zheng, D. Zhuo, L. Wu, Z. Weng, 3D printing of high viscosity UV-Curable resin for highly stretchable and resilient elastomer, Adv. Mater. 35 (2023), https://doi.org/10.1002/adma.202304430.
[54] J. Shan, Z. Yang, G. Chen, Y. Hu, Y. Luo, X. Dong, W. Zheng, W. Zhou, Design and synthesis of free-Radical/Cationic photosensitive resin applied for 3D printer with liquid crystal display (LCD) irradiation, Polymers 12 (2020) 1346, https://doi.org/10.3390/polym12061346.
[55] S. Chen, Y. Duan, W. Hua, Q. Lin, B. Qu, R. Wang, Y. Zheng, X. Liu, W. Li, D. Zhuo, Synthesis of novel acrylic liquid-crystal resin and its in-situ enhancement in light-curing 3D printing performance, J. Mater. Res. Technol. 17 (2022) 2158–2174, https://doi.org/10.1016/j.jmrt.2022.01.159.
[56] M. Lebedevaite, A. Gineika, V. Talacka, K. Baltakys, J. Ostrauskaite, Development and optical 3D printing of acrylated epoxidized soybean oil-based composites with functionalized calcium silicate hydrate filler derived from aluminium fluoride production waste, Composites Part A Appl Sci Manuf 157 (2022) 106929, https://doi.org/10.1016/j.compositesa.2022.106929.
[57] D. Mondal, Z. Haghpanah, C.J. Huxman, S. Tanter, D. Sun, M. Gorbet, T.L. Willett, mSLA-based 3D printing of acrylated epoxidized soybean oil - nano-hydroxyapatite composites for bone repair, Mater. Sci. Eng. C 130 (2021) 112456, https://doi.org/10.1016/j.msec.2021.112456.
[58] W. Feng, L. Chang, J. He, Z. Dai, X. Shi, W. Xie, F. Xu, A nanomodified-ultrasonic method to improve the shear strength of adhesively bonded composite joints, Composites Part A Appl Sci Manuf 187 (2024) 108483, https://doi.org/10.1016/j.compositesa.2024.108483.
[59] H. Ejaz, A. Mubashar, E. Uddin, Z. Ali, N. Arif, Influence of MWCNTs on strength properties of high viscous epoxy adhesive and fracture behavior of adhesively bonded joints, Theor. Appl. Fract. Mech. 120 (2022) 103412, https://doi.org/10.1016/j.tafmec.2022.103412.
[60] F. Gojny, M. Wichmann, B. Fiedler, K. Schulte, Influence of different carbon nanotubes on the mechanical properties of epoxy matrix composites – a comparative study, Compos. Sci. Technol. 65 (2005) 2300–2313, https://doi.org/10.1016/j.compscitech.2005.04.021.
[61] T. Zhou, X. Wang, H. Zhu, T. Wang, Influence of carboxylic functionalization of MWCNTs on the thermal properties of MWCNTs/DGEBA/EMI-2,4 nanocomposites, Composites Part A Appl Sci Manuf 40 (2009) 1792–1797, https://doi.org/10.1016/j.compositesa.2009.08.019.
[62] M. Theodore, M. Hosur, J. Thomas, S. Jeelani, Influence of functionalization on properties of MWCNT–Epoxy nanocomposites, Mater. Sci. Eng., A 528 (2011) 1192–1200, https://doi.org/10.1016/j.msea.2010.09.095.
[63] M.R. Saeb, E. Bakhshandeh, H.A. Khonakdar, E. Mäder, C. Scheffler, G. Heinrich, Cure kinetics of epoxy nanocomposites affected by MWCNTs functionalization: a review, Sci. World J. 2013 (2013), https://doi.org/10.1155/2013/703708.